



UNIVERSITY OF LEEDS

This is a repository copy of *Local structural analysis of erbium-doped tellurite modified silica glass with x-ray photoelectron spectroscopy*.

White Rose Research Online URL for this paper:  
<http://eprints.whiterose.ac.uk/148706/>

Version: Accepted Version

---

**Article:**

Kamil, SA, Chandrappan, J, Portoles, J et al. (2 more authors) (2019) Local structural analysis of erbium-doped tellurite modified silica glass with x-ray photoelectron spectroscopy. *Materials Research Express*, 6 (8). ARTN 086220. ISSN 2053-1591

<https://doi.org/10.1088/2053-1591/ab28eb>

---

© 2019 IOP Publishing Ltd. This is an author produced version of a paper published in *Materials Research Express*. Uploaded in accordance with the publisher's self-archiving policy.

**Reuse**

Items deposited in White Rose Research Online are protected by copyright, with all rights reserved unless indicated otherwise. They may be downloaded and/or printed for private study, or other acts as permitted by national copyright laws. The publisher or other rights holders may allow further reproduction and re-use of the full text version. This is indicated by the licence information on the White Rose Research Online record for the item.

**Takedown**

If you consider content in White Rose Research Online to be in breach of UK law, please notify us by emailing [eprints@whiterose.ac.uk](mailto:eprints@whiterose.ac.uk) including the URL of the record and the reason for the withdrawal request.



[eprints@whiterose.ac.uk](mailto:eprints@whiterose.ac.uk)  
<https://eprints.whiterose.ac.uk/>

# Local structural analysis of erbium-doped tellurite modified silica glass with X-ray photoelectron spectroscopy

Suraya Ahmad Kamil<sup>a,\*</sup>, Jayakrishnan Chandrappan<sup>b</sup>, Jose Portoles<sup>c</sup>, Paul Steenson<sup>d</sup>, Gin Jose<sup>e</sup>  
<sup>a</sup>School of Physics and Material Studies, Faculty of Applied Sciences, Universiti Teknologi MARA,  
40450 Shah Alam, Selangor, Malaysia

<sup>b</sup>Centre for Process Innovation Limited (CPI), Neville Hamlin Building, NETPark, Thomas Wright Way,  
Sedgefield, County Durham, TS21 3FG, UK

<sup>c</sup>National EPSRC XPS Users' Service (NEXUS), School of Mechanical and Systems Engineering,  
Newcastle University, Newcastle upon Tyne, Tyne and Wear NE1 7RU, UK

<sup>d</sup>Institute of Microwave and Photonics, School of Electronics and Electrical Engineering, University of  
Leeds, Leeds LS2 9JT, UK

<sup>e</sup>Applied Photon Science, School of Chemical and Process Engineering, University of Leeds, Leeds  
LS2 9JT, UK

\*corresponding author: [suraya\\_ak@uitm.edu.my](mailto:suraya_ak@uitm.edu.my)

## Abstract

Ultrafast laser plasma doping (ULPD) is a recently developed technique that enables the blending of femtosecond laser produced plasma from a TeO<sub>2</sub> (target) based glass with a SiO<sub>2</sub> (substrate) without or minimum phase separation to form a silicate glass. The background oxygen gas pressure plays a major role in ULPD as it directly impacts the plasma plume characteristics, resulting in lower erbium doped tellurite modified silica (EDTS) thickness and refractive index at higher process gas pressure. X-ray photoelectron spectroscopy (XPS) used in this study to analyse the formation of EDTS and local bonding environment of its constituents. This report confirms the presence of both target materials and SiO<sub>2</sub> in the resulting EDTS films. XPS of O 1s core, confirms that bridging oxygen (BO) is more dominant compared to non-bridging oxygen (NBO) in the EDTS glass network, and the amount of BO is more stand out for higher gas pressures when the glass modifiers are relatively smaller in concentration. Our study revealed the nucleation Te and Er to form metal nanoparticles in glass under certain preparation conditions/doping concentration which were previously undetected using other experimental techniques. It is important to control this nanoparticle formation in engineering EDTS for photonic device applications.

Keywords: XPS, ultrafast lasers, laser ablation, optical materials, Er<sup>3+</sup>-doped glasses

## 1.0 Introduction

Many studies have been undertaken on silica ( $\text{SiO}_2$ ) glass material due to its tremendously compelling properties and plentiful applications for ultra-high bandwidth fibre optic communications which underpin modern society [1,2]. One of the fascinating properties of this material is its excellent transparency from infrared (IR) to ultraviolet (UV) range making it invaluable for photonic applications such as optical telecommunications, optoelectronic devices, medical applications, and a wealth of sensors [1,3,4]. The realisation of optical amplifiers operating in the  $\text{Er}^{3+}$  emission band (1530-1550 nm) was made possible by the doping of erbium into  $\text{SiO}_2$  and widely used as efficient signal boosters for the long-haul optical network [5,6]. However, the solubility of erbium in silica is very low due to the mismatch in valency and the difference in ionic radii between the  $\text{Er}^{3+}$  and elements of silica. These differences cause the Er to cluster in the silica matrix even at a moderate concentration leading to a less than ideal solubility limit and reduced optical amplifier potential [7]. Using the ultrafast laser plasma doping technique (ULPD) approach, a very attractive mixture of  $\text{SiO}_2$  and high concentration erbium-doped  $\text{TeO}_2$  based glass has been achieved which promises to offer a potential solution for the limited solubility issue of erbium in silica [8,9].

The ULPD technique has been shown to assist the blending of  $\text{SiO}_2$  and  $\text{TeO}_2$  based glasses without or minimum suffering phase separation, and this combination of glasses ( $\text{SiO}_2$  and  $\text{TeO}_2$ ) seems not to have been widely reported. This may be due to phase separation that occurred in a ternary or quaternary glass as reported in glass system  $\text{TeO}_2\text{-B}_2\text{O}_3\text{-SiO}_2$  [10],  $\text{Li}_2\text{O-TeO}_2\text{-SiO}_2$  [11] and  $\text{TeO}_2\text{-SiO}_2\text{-ZnO-K}_2\text{O}$  [12] which in turn, made it less enticing to be studied. The previous phase separation is thought to be due to the presence of  $\text{Te}^{4+}$  ions. The high polarizability of the  $\text{Te}^{4+}$  ions is thought to distort the Te-O and O-Si-O bonds and the presence of NBO will accelerate the bond breaking and promote phase separation [13].

The mixture of these two  $\text{SiO}_2$  and  $\text{TeO}_2$  based glasses fabricated by ULPD is referred to as erbium-doped tellurite modified silica (EDTS), and has been extensively studied regarding its

optical and structural properties and their dependency on process parameters such as; fs-laser energy, repetition rate, and target glass composition [8,9]. However, the dependency of the properties on background gas pressure is yet to be fully investigated and understood especially with regards to its effect on the resulting chemical properties of the SiO<sub>2</sub> and TeO<sub>2</sub> mixture. Background gas pressure has been found to be a key process parameter in the ULPD technique, at least for this mixture. Ambient gas present during ULPD process will scatter, attenuate and thermalize the ion energies in the plasma plume, and by carefully controlling the gas pressure in the chamber, it can influence the kinetic energy and mean free path of the ablated ions/nanoparticles which results in important changes in EDTS properties [14,15].

In this present paper, the chemical analysis of EDTS with respect to different oxygen (O<sub>2</sub>) gas pressures was achieved using X-ray photoelectron spectroscopy (XPS). This technique has been employed to elucidate the elemental surface composition, the oxidation state of the cations and the nature of oxygen bonding [16,17]. Indeed, XPS is able to resolve the contribution of bridging oxygen (BO) and non-bridging oxygen (NBO) peak in O 1s core level spectra in binary and complex oxide glass system [16–18]. Based on the XPS analysis, a local structure of EDTS could be estimated. In addition, a depth profiling during XPS measurement is important in order to investigate the distribution of various elements in EDTS as a function of EDTS layer thickness.

## **2.0 Experimental procedures**

### **2.1 Sample preparations**

The EDTS was processed via ULPD with silica-on-silicon (SOS) as the underlying substrate. The initial thickness of silica layer was 1 μm. A femtosecond (fs) laser (100 fs-pulsed, wavelength of 800 nm, energy of 50 μJ and repetition rate of 1 kHz) was used to ablate the target material (79.5%TeO<sub>2</sub>-10%Na<sub>2</sub>O-10%ZnO-0.5%Er<sub>2</sub>O<sub>3</sub> (Er-TZN)). The target material was fabricated using a standard glass melt-quenching technique [19]. The fs-laser was guided into the vacuum chamber and then focused on the flat target surface at 60° angle from normal,

which was then rastered and rotated to ensure uniform target ablation and to produce consistent ablation plume. After cleaning (using deionised water, acetone and ultrasound), the SOS substrate was then loaded into the deposition chamber and positioned 70 mm above and normal to the target. Subsequently, the ablation chamber was pumped down to  $8 \times 10^{-6}$  mTorr or lower, before establishing oxygen background gas. The substrate was heated to 570 °C and then exposed to the fs-laser plasma plume for four hours in a background oxygen gas to obtain EDTS layer. Four samples H50, H70, H90 and H100, they were fabricated at O<sub>2</sub> pressures of 50, 70, 90 and 100 mTorr respectively.

## 2.2 Sample characterizations

The cross-section and thickness of modified layer were obtained using a Hitachi SU8230 scanning electron microscope (SEM). A prism coupler method was employed to verify the thickness of EDTS and measure the EDTS refractive index. A Philips X'Pert X-ray diffraction (XRD) tool was utilised to investigate any crystalline phases that might exist in EDTS. Surface analysis was carried out using an XPS (K-alpha XPS instrument (Thermo Scientific)), with a monochromatic Al K $\alpha$  (1486.6 eV) source. For the initial survey spectra, a pass energy of 150 eV with the step size of 0.4 eV was used, while for the high-resolution spectra, a pass energy of 40 eV with a step size of 0.1 eV was applied. Analysis and peak fitting were performed using CasaXPS software. A Shirley background subtraction and a mixed of Gaussian-Lorentzian function were utilized to fit all the peak in the obtained spectra. **Since XPS data is derived not only originating from the photoemission process but also influenced by the instrument and broadening from slightly different local bonding [20], therefore the mix Gaussian-Lorentzian function is suitable and widely used for the XPS peak fitting.** All reported binding energies (BE) of photoelectron spectra in this work used C 1s peak at 285 eV as a reference to maintain the consistency and correction for sample charging. The C 1s peak is an adventitious peak that obtained from unavoidable hydrocarbon contaminants in most vacuum chambers, and is generally accepted to be independent of the chemical state of the

material under study [21,22]. Depth profiling was also employed using 3 keV Ar<sup>+</sup> sputtering to quantify the chemical composition as a function of depth.

### **3.0 Results and discussions**

Fig. 1 (a)–(d) represents the backscattered (BSE) SEM cross-section image of the samples H50, H70, H90 and H100 fabricated using various background O<sub>2</sub> pressures and showing that the EDTS thickness increases with lower oxygen gas pressure, with all other parameters remaining constant. This confirms that the EDTS film characteristics were influenced by the oxygen pressure used. Generally, plasma plume can be distributed much more widely when background gas is present during the ablation process. Since the target material used was an oxide-based glass and the substrate was SiO<sub>2</sub>, oxygen was chosen as the background gas to ensure an oxygen-rich environment surrounding the deposition plume and facilitating the bonding between elements from Er-TZN and SiO<sub>2</sub>. The background pressure did not affect the path or laser beam absorption, even though the plasma plume characteristics depended heavily on background gas pressure. Reduction in gas pressure increased the kinetic energy of the ablated species [23]. Thus, the collision rate between the ablated species (Er-TZN) and the O<sub>2</sub> species during their flight to substrate reduced which in turn allowed more Er-TZN ions to reach and penetrate into silica layer. The outcome was penetration of Er-TZN elements into silica became more aggressive thus the EDTS thickness increased at a decreased oxygen gas pressure. The visible thickness as measured using SEM for the samples is shown in Table 1.

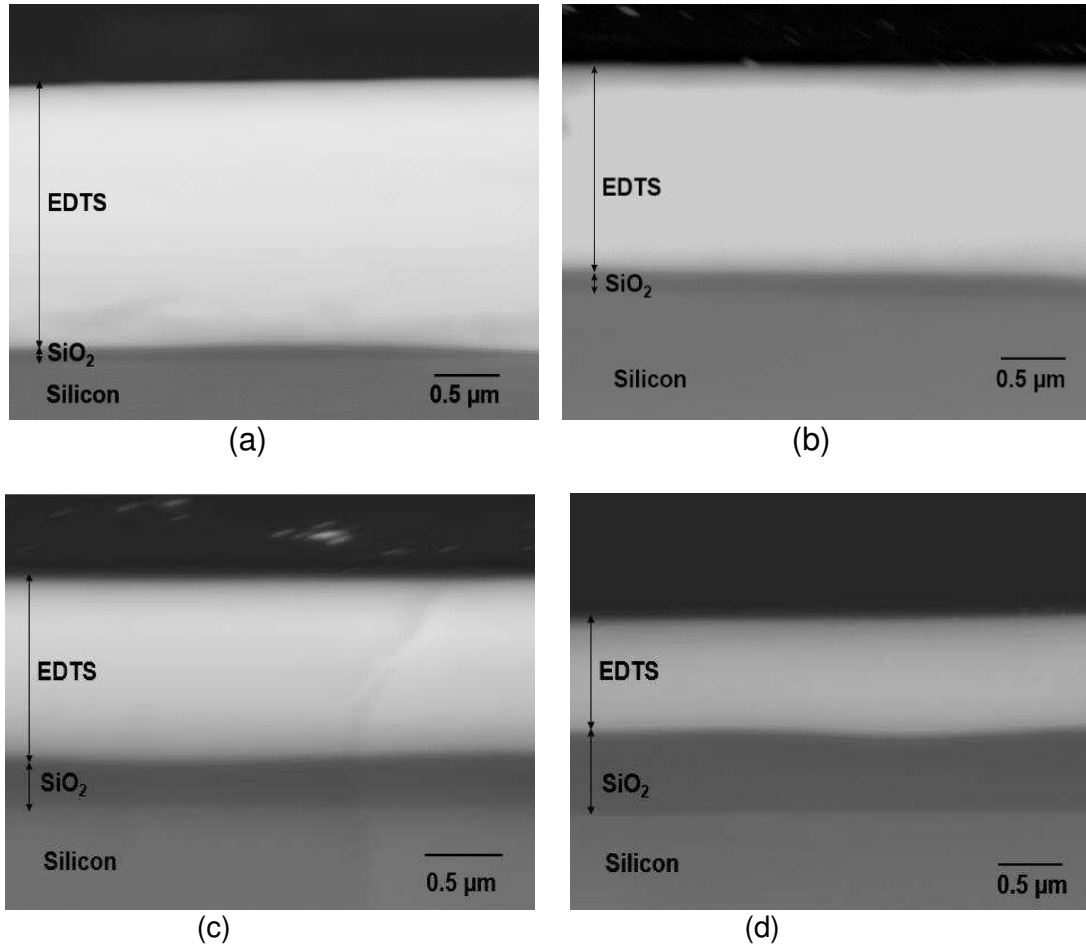


Fig. 1: Backscattered cross-section SEM image of SOS doped with Er-TZN at a background oxygen gas pressure of (a) 50 mTorr (H50) (b) 70 mTorr (H70) (c) 90 mTorr (H90) and (d) 100 mTorr (H100).

Table 1: EDTS layer and remaining silica underneath EDTS thickness and refractive index measured by SEM and prism coupler for the sample prepared using various oxygen gas pressure.

Sample	EDTS thickness measured with SEM ( $\mu\text{m}$ )	EDTS thickness measured with prism coupler ( $\mu\text{m}$ )	$\text{SiO}_2$ thickness below EDTS layer measured with SEM ( $\mu\text{m}$ )	Refractive Index
H50 (50 mTorr)	$1.86 \pm 0.03$	$1.71 \pm 0.01$	$0.07 \pm 0.01$	$1.6484 \pm 0.0001$
H70 (70 mTorr)	$1.64 \pm 0.09$	$1.67 \pm 0.03$	$0.13 \pm 0.03$	$1.6356 \pm 0.0009$
H90 (90 mTorr)	$1.12 \pm 0.07$	$1.18 \pm 0.01$	$0.27 \pm 0.03$	$1.5990 \pm 0.0003$
H100 (100 mTorr)	$0.81 \pm 0.05$	$0.85 \pm 0.02$	$0.57 \pm 0.05$	$1.5987 \pm 0.0003$

Reduction of the EDTS thickness and refractive index as a function of O<sub>2</sub> pressure was also measured using prism coupler technique (Table 1). The EDTS refractive index decreases with increase in oxygen gas pressure. This relationship seems reasonable because lower gas pressure corresponds to a higher kinetic energy which also correlates to higher plasma density. The plasma density and gas pressure correlation is related with Beer's law behaviour which is given by  $I = I_0 \exp - P\sigma x$ , where  $I$  is plasma density,  $I_0$  is initial plasma density at the target,  $P$  is the oxygen ambient gas pressure,  $\sigma$  is the total cross-section for plasma-to-oxygen collisions and the  $x$  is the distance from the target. The resulting plasma density is believed to obey a Beer's law trend where the density of the plasma is exponentially reduced as the background gas pressure increases [24]. Consequently, less elements from Er-TZN can be integrated into the silica on the substrate surface resulting low dense layer of EDTS when the higher O<sub>2</sub> gas pressure was used. This inverse relationship between refractive index and background process gas pressure was also reported elsewhere [25–28].

Fig. 2 presents the XRD pattern for the samples fabricated using oxygen pressures of; 70 mTorr (H70), 90 mTorr (H90) and 100 mTorr (H100) and did not show any distinct peaks except for that at  $2\theta = 69^\circ$  corresponding to the underlying silicon, Si (100) of SOS substrate. It showed that the thin films were all amorphous with a diminishing broad spectrum of silicate with increased oxygen gas pressure and caused by fewer Er-TZN ions that penetrated the silica. The broad silicon peak at  $2\theta = 69^\circ$  is probably due to the defects that originates from the effects of thermal oxidation of silicon. At the interface region of Si-SiO<sub>2</sub>, there will be at least one layer of silicon atoms that are bonded both with oxygen and silicon atoms. These silicon atoms are in the intermediate oxidation states (+1, +2, +3, depending on the number of oxygen atoms they are bound) [29,30]. The presence of these silicon atoms with intermediate states are source of defects [31] which can make the intermediate layer become disordered. As the beam penetration depth is probable limited to the intermediate layer, this results in the producing of broad peak in XRD patterns.

The H50 sample, exhibited a mixed amorphous-crystalline phase. There were crystallite peaks at  $2\theta$  of  $23.05^\circ$ ,  $27.62^\circ$ ,  $38.40^\circ$ ,  $40.44^\circ$ ,  $43.31^\circ$ ,  $46.22^\circ$ ,  $49.62^\circ$ ,  $51.28^\circ$ ,  $56.88^\circ$ ,  $62.95^\circ$ , and  $82.19^\circ$  which implied the presence of Te. The Te has a hexagonal structure and belongs to the P3121 (152) space group (ICDD reference code: 00-036-1452). This peak is strongly believed to be due to Te crystallites particles situated at the interface between EDTS and silicon as shown in Fig. 3. The crystallite particles formation is due to the failure of elements from Er-TZN to penetrate silicon and accumulated at the silica-silicon interface. The excess Te which cannot form network with the modified silica layer undergoes nucleation. Er-TZN which was rich with oxygen would have difficulty to create any bond in silicon due to the absence of oxygen in silicon. Hence it preferred to remain in areas that were abundant with oxygen. Phase separation between those materials also could be the reason for the appearance of this crystallite particles.

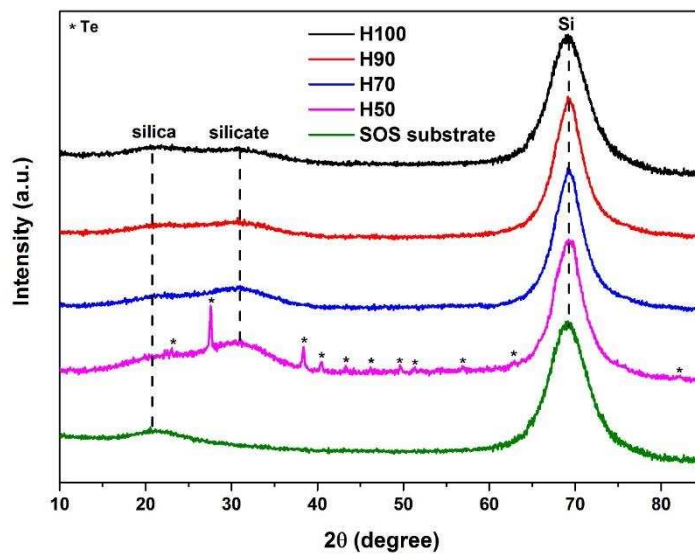


Fig. 2: XRD spectra of SOS substrate and samples prepared using different oxygen gas pressure.

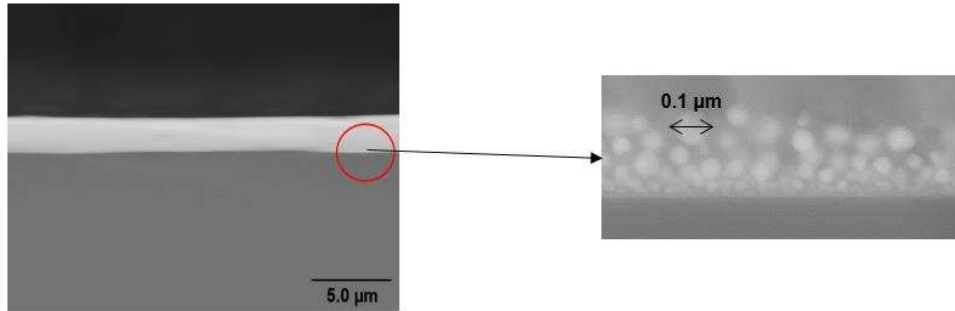


Fig. 3: Crystallite particle at the interface between silicon and EDTS at the area when 50 mTorr oxygen gas pressure used (H50). The appearance of crystallite particle is not visible for other samples under same magnification.

From the XPS survey scan, as shown in Fig. 4, surface EDTS once again proved that it was a mixture of elements from target materials (except erbium) and silica from the substrate. The Er concentration was too low to be detected by survey scan. Erbium is commonly detected from Er 4d peak, but it was overshadowed by the more prominent background Si 2s peak due to the much higher Si concentration compared to Er. The absence of distinctive peaks other than peaks for carbon (C 1s) and species from silica and Er-TZN (except erbium) in the survey spectra, showed that there was no contaminant present at the surface of EDTS. The intensity of Na 1s, Te 3d and Zn 2p is the highest for sample H50 supporting the hypothesis that at low O<sub>2</sub> pressures more elements from target glass get embedded in the SOS.

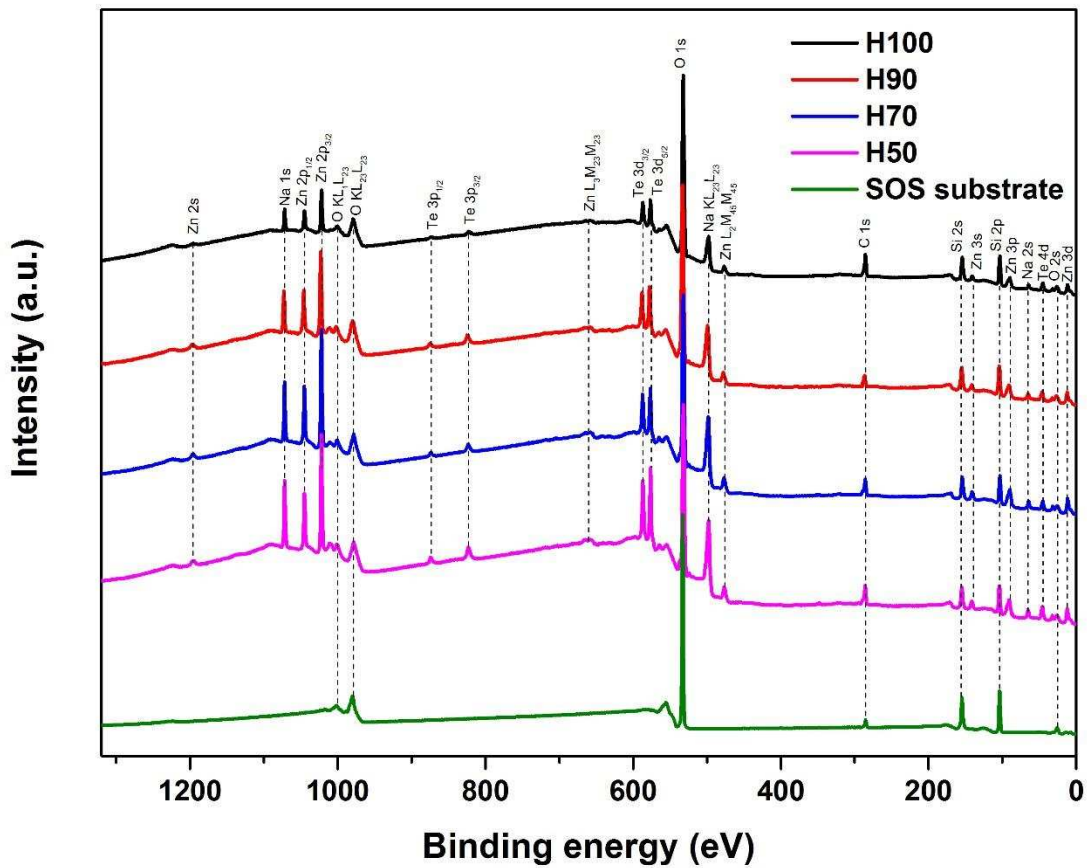


Fig. 4: XPS survey scans from the surface of the SOS substrate and samples H50, H70, H90, and H100 using monochromatic Al K $\alpha$  (1486.6 eV).

As the survey scan failed to detect the presence of erbium, a high-resolution scan for the core level of O 1s, Si 2p, Te 3d, Zn 2p, Na 1s and Er 4p $_{3/2}$  was undertaken to determine the elemental composition present at EDTS surface. Table 2 shows the elemental concentration for sample H50, H70, H90 and H100 surface. The presence of Si and target material at EDTS surface confirm that there is a mixing of target and substrate components. Table 2 clearly showed an increase in O and Si while a decline of Te, Zn, Na and Er for samples prepared with higher O $_2$  pressure. This trend in elemental composition was manifested in the decrease of refractive index as tabulated in Table 1. [When the gas pressure is high, collisions between the species in the plasma plume and gas molecule are relatively more frequent \[32\]. This condition causes the energy of the species in plasma plume to decrease and also causes](#)

more species to get deflected. Therefore, less elements in the Er-TZN were able to penetrate the substrate and subsequently reduce the density and refractive index of the EDTS.

Table 2: Elemental composition of EDTS layer surface for samples H50, H70, H90 and H100 obtained from a high-resolution scan. The estimated uncertainty is  $\pm 0.01$  at. %.

Elements	Sample H50 (at. %)	Sample H70 (at. %)	Sample H90 (at. %)	Sample H100 (at. %)
O	54.94	55.83	58.61	61.97
Si	23.74	24.85	26.81	27.53
Na	10.07	9.47	6.75	4.52
Zn	6.61	6.02	4.44	3.61
Te	3.47	2.86	2.77	1.78
Er	1.17	0.97	0.62	0.59

Fig. 5 (a)-(c) showed the high-resolution scan and the fitted peak for O 1s spectrum. As seen in Fig. 5, the spectra consisted of bridging oxygen (BO) and non-bridging oxygen (NBO) components which were situated at the binding energy (BE) of  $\sim 532$  eV and  $\sim 530$  eV, respectively. If an oxygen is involved in the glass network linking two glass former as in -Si-O-Si- it is called a bridging oxygen while a non-bridging oxygen is one which is bonded with a network former and a network modifier as in -Si-O: Na. Apart from BO and NBO peak, there was a Na  $KL_1L_{2,3}$  peak at  $\sim 536$  eV which arose due to Auger process and is not associated with O 1s. The conclusions pertaining to the NBO and BO peaks are consistent with electronegativity and electron density arguments. Value for electronegativity for oxygen, silicon, tellurium, zinc, sodium, and erbium are 3.44, 1.90, 2.10, 1.65, 0.93 and 1.24 respectively. BO peak always had higher BE than NBO as BO was bonded with glass former such as Si and Te which had higher electronegativity compared to Na and Er that were glass modifiers. Higher electronegative elements would attract electrons towards it while forming bonds with O. This made the reduction of electron density around the BO causing the binding energy of the core electrons to increase. As a result, BE for BO is higher comparing to NBO.

The best fitting result from the O 1s spectra were displayed in Table 3. From Fig. 5 and Table 3, it could be seen that BO looked more dominant than NBO in the EDTS network. The position of BO and NBO peaks of O 1s spectra from this work was similar to other silicate glasses that had been reported [17,33,34]. This evidence again supported that elements from the target material had penetrated and mixed with the silica layer resulting in a silicate glass. The concentration of Si that acted as a main glass former in EDTS network was far higher than other cations which caused BO to be dominant in EDTS. However, the amount of NBO was increasing when lower background gas pressure was used due to more glass modifier elements present in the doped layer. The increment of these modifier atoms also caused O 1s peak shift to lower BE as shown in Fig. 5 and Table 3 due to the average increased electron population at the oxygen atoms.

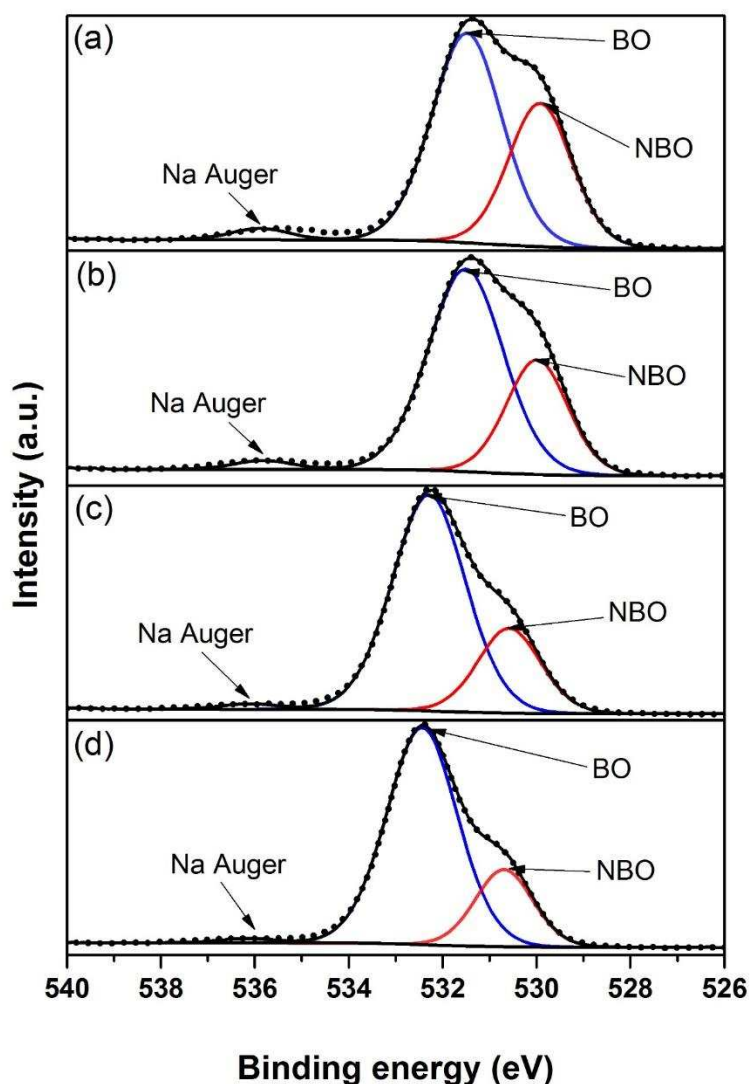


Fig. 5: High-resolution core level spectra of the O 1s of the surface of EDTS layer for samples prepared under background O<sub>2</sub> pressure of (a) 50 mTorr (H50) (b) 70 mTorr (H70) (c) 90 mTorr (H90), and (d) 100 mTorr (H100).

Table 3: Fitted peak information for BO and NBO resulting from O 1s core level of EDTS for samples H50, H70, H90 and H100.

Sample	Peak position (eV)		Area (%)	
	BO	NBO	BO	NBO
H50	531.48	529.93	61.90	38.10
H70	531.51	529.99	68.35	31.65
H90	532.29	530.58	74.84	25.16
H100	532.44	530.69	77.44	22.56

Fig. 6 shows de-convoluted Si 2p core level peaks for samples prepared at different oxygen gas pressures. Each Si 2p peak consisting of two peaks which were 2p<sub>1/2</sub> and 2p<sub>3/2</sub> due to

spin-orbit splitting. These two peaks have been fitted with area ratio  $2p_{1/2}/2p_{3/2} = 1/2$  based on the theory of splitting of the 2p level. The BE for both peaks for different  $O_2$  pressures are shown in Table 4. Si  $2p_{1/2}$  and Si  $2p_{3/2}$  appear to be shifted to lower BEs for samples fabricated using lower  $O_2$  pressures. The drop in the BE is attributed to the increase in number of Si atoms which were attached to a non-bridging oxygen atom. NBO bonded with Na, Zn or Er had higher ionicity compared to Si which is covalently bonded with NBO. This caused oxygen to relax its attractive potential against the Si atom which in turn resulted in an increase in electron density for the Si-O tetrahedron. Correspondingly, an increase in electron density on Si atom caused the BE for Si 2p to decrease [34,35]. Therefore, with the increase in Na, Zn, and Er in the EDTS, due to the lower use of  $O_2$  pressure, the BE for Si 2p decreases. Although Te has a higher electronegativity than Si and the potential Si-O-Te bond might cause electron population decrease at Si, but its lower concentration than Na and Zn might overshadow its role.

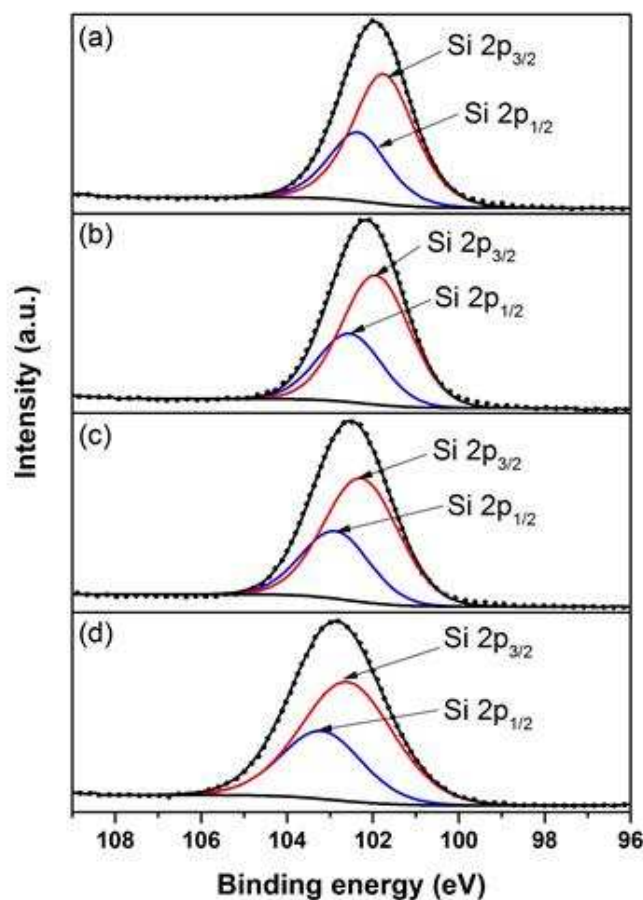


Fig. 6: High-resolution Si 2p spectra of the surface of EDTS layer for sample (a) H50 (b) H70 (c) H90, and (d) H100

Table 4: XPS binding energy for the core levels of Si 2p, Na 1s and Zn 2p for samples H50, H70, H90, and H100.

Sample	Si 2p		Na 1s	Zn 2p	
	Si 2p <sub>1/2</sub>	Si 2p <sub>3/2</sub>		Zn 2p <sub>1/2</sub>	Zn 2p <sub>3/2</sub>
H50	102.35	101.75	1071.67	1044.82	1021.74
H70	102.54	101.94	1071.35	1044.43	1021.34
H90	102.88	102.28	1070.86	1044.11	1021.02
H100	103.20	102.60	1070.55	1043.84	1020.77

No deconvolution of the spectra was required for Na 1s (Fig. 7) as it had no spin-orbit splitting for orbital s. From Table 4 and Fig. 7, Na 1s peak had been observed to shift to lower BEs for samples corresponded to the increase in background gas pressure. It is argued that Na, which was the most electropositive element in the doped layer encourages the electrons to congregate at the NBO sites. Due to this, electron density was lower around the Na further increasing the attraction force between the nucleus and O 1s electrons and also increasing the Na 1s binding energy. Consequently, the sample with higher concentration of Na tends to exhibit higher BE.

The Zn 2p was similarly fitted like peak Si 2p without need of deconvolution as Zn 2p<sub>1/2</sub> and Zn 2p<sub>3/2</sub> are non-overlapping (Fig. 8). Table 4 shows that the Zn 2p peak shifts in the opposite direction to the Si 2p, as for EDTS, the Zn atom acted as a modifier like Na. The Zn behaves is similarly to Na, due to its high electropositive, electron density to be reduced around the Zn atoms causing them resulting in higher BE. Consequently, the reduction in Zn for samples prepared under higher O<sub>2</sub> pressures (Table 2) resulted in the H100 sample exhibiting the lowest BE (Fig. 8).

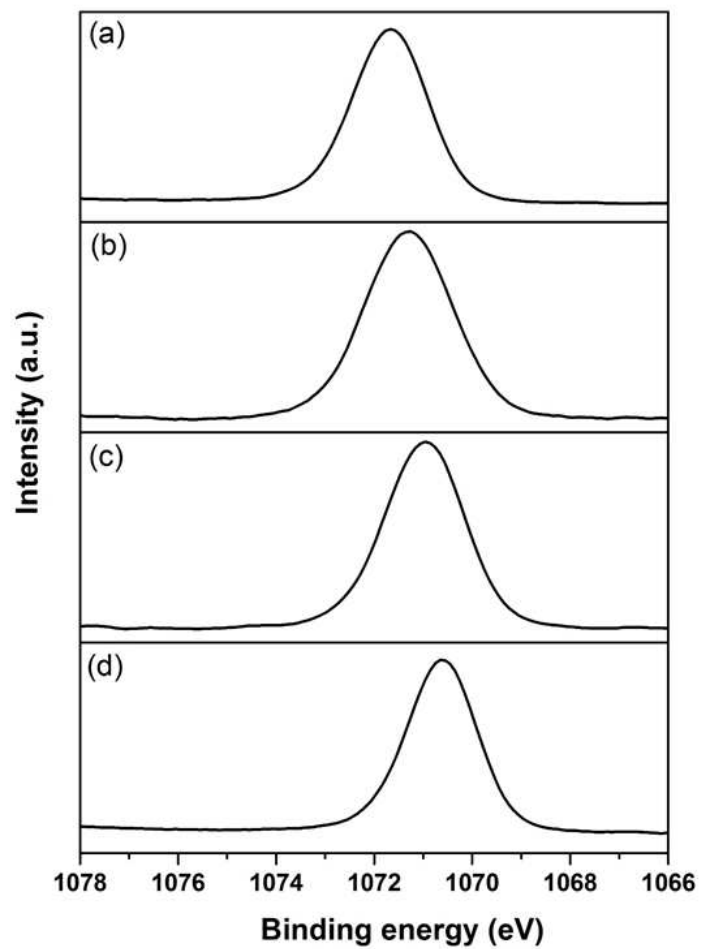


Fig. 7: High-resolution Na 1s XPS spectra of the surface of EDTS layer for the sample (a) H50 (b) H70 (c) H90 and (d) H100

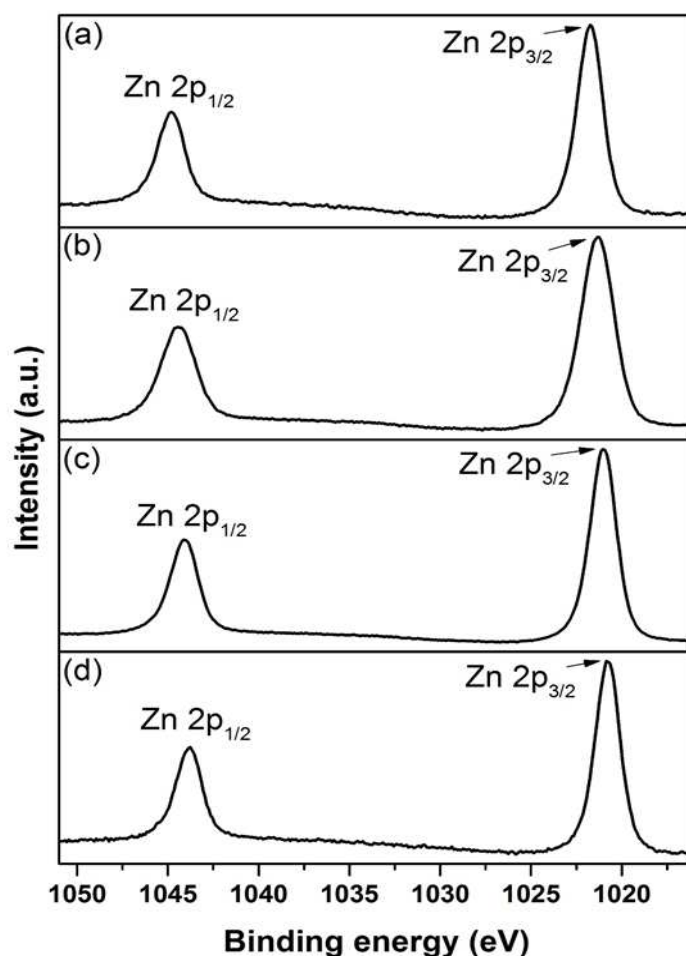


Fig. 8: Zn 2p photoelectron peaks of the samples (a) H50 (b) H70 (c) H90, and (d) H100 showing the spin-orbit split into the Zn 2p<sub>3/2</sub> and Zn 2p<sub>1/2</sub> level.

The XPS of Te 3d<sub>5/2</sub> show two distinct peak that corresponded to Te oxide and Te metal as shown in Fig. 9. From the Te oxide peak, deconvolution revealed the presence of TeO<sub>4</sub> and TeO<sub>3</sub> polyhedra. In TeO<sub>4</sub>, Te are bonded to BOs while for each TeO<sub>3</sub>, Te is bonded to an NBO. As clearly shown in Fig. 9 and Table 5, the proportion of Te atoms which were bonded to NBO was much higher than bonded to BO. This clearly showed the difficulty that Te experiences bonding with -Si-O- to form -Si-O-Te- linkages. As a glass former in itself it would be easier for Te to bond with Si-O in the presence of a modifier elements which would promote the rupture of strong -Si-O-Si- covalent bonds. However, the number of BO was clearly higher for samples prepared using the lower background O<sub>2</sub> pressure, probably because the Te ions had higher kinetic energy at lower gas pressure and consequently were more capable of breaking Si-O-Si bonds and attaching to BO. Consequently, H50 exhibited the highest

proportion of  $\text{TeO}_4$  as clearly evident from Table 4. On the other hand, when the total amount of Te decreased in proportion to modifier ions for samples prepared with higher background  $\text{O}_2$  pressures the  $\text{TeO}_3$  units increased as expected. This explains the relatively larger shift for BE of Te in  $\text{TeO}_3$  comparing to  $\text{TeO}_4$ .

Interestingly, Te metal peaks were also detected in the XPS of EDTS as shown in Fig. 9. Because EDTS is amorphous [8,9], the presence of Te metal appeared to be undetectable by XRD (Fig. 2) and this can be inferred that the Te metal particles were embedded in the glass matrix and their size is below XRD detection limit ( $> 5$  nm) [36,37]. As for the BE of Te metal, it showed a similar trend with Te oxide. The proportional reduction in BE for the Te metal with increasing  $\text{O}_2$  pressure increment was believed to be related to size of the metal particles. As femtosecond laser produced plasma of the target glass consists predominantly of nanoparticles [38] a reasonable assumption is that these Te metal nanoparticles are formed post deposition within the silica due to diffusion and nucleation. It is the excess of Te present in the EDTS that cannot participate in glass network that made it nucleate and grow. The use of high pressure caused a higher incidence of collision to occur by vapor species and the nucleation and growth of these vapor species promoted the formation of particulates. Increased gas pressure caused velocity vapor species to decrease, which in turn, caused the particulates to become larger when they reached the substrate. Based on Fig. 9 and Table 5, it is clear that H50 have higher BE and this is related to its smaller particle distribution as discussed above. This relationship between particle size and BE had been reported in the literature for other type of metal nanoparticles [39–41]. It is to do with relaxation energy of X-ray photoelectron in a metal nanoparticle. In a nanoparticle the relaxation following photoemission from an atom take place by the rearrangement of the electron from within the atom (intra-atomic relaxation) and the movement of electron among the neighbouring atoms (extra-atomic relaxation) [42]. This relaxation energy produced due to the movement of electrons to the lower energy level helps increase the kinetic energy of the ejected photoelectron and at the same time decrease the binding energy [43,44]. When the particle

size became smaller, the number of overlapping energy levels decreased, and the band gap became larger. The relationship between band gap and particle size could be simplified by Brus equation [45,46] (with the assumption that nanoparticles were in spherical form):

$$E_g^* = E_g^{\text{bulk}} + \frac{h}{8r^2} \left( \frac{1}{m_e^*} + \frac{1}{m_h^*} \right) - \frac{1.8e^2}{4\pi\epsilon\epsilon_0 r} \quad (1)$$

Here,  $E_g^*$  is the band gap of nanoparticle,  $E_g^{\text{bulk}}$  is the band gap of bulk material (for Te is 0.33 eV),  $h$  is Planck constant,  $r$  is nanoparticle radius,  $m_e^*$  is effective mass of electrons,  $m_h^*$  is effective mass of holes,  $e$  is standard unit charge,  $\epsilon_0$  is permittivity of free space and  $\epsilon$  is relative permittivity of the solid. From equation (1), again it shows that band gap increased when the particle size is decreased. In smaller particles the wider band gap makes it more difficult for electrons to fall to the lowest occupied level and this caused the likelihood of relaxation process to be low. When the relaxation process lower, the kinetic energy of photoelectron decrease proving increased binding energy of the metal particle [47].

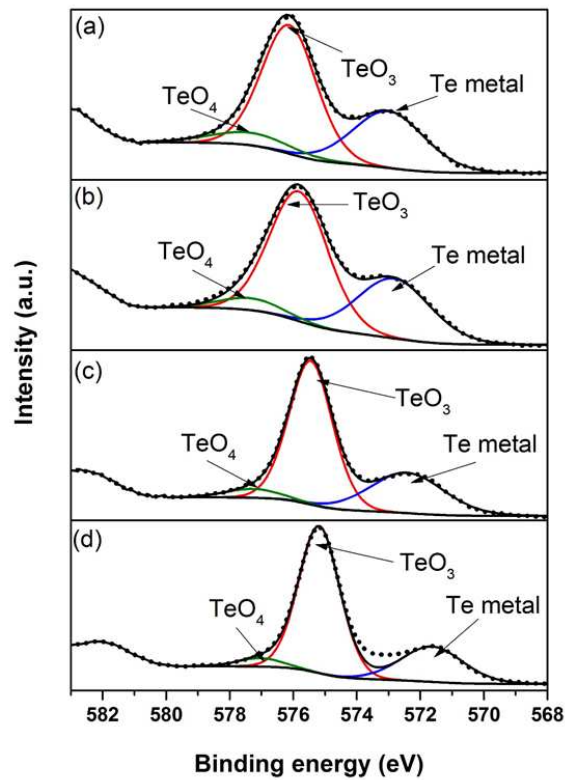


Fig. 9: Te 3d<sub>5/2</sub> spectrum of the surface of EDTS layer for the sample (a) H50 (b) H70 (c) H90 and (d) H100. From the fitted peak suggest that EDTS contains Te metal and two form of Te oxide which are TeO<sub>3</sub> and TeO<sub>4</sub>.

Table 5: Peak positions (eV) and areal percentage (%) for the component in core level Te 3d<sub>5/2</sub>.

Sample	Te 3d <sub>5/2</sub>					
	Peak position (eV)			Area (%)		
	Te oxide (TeO <sub>4</sub> )	Te oxide (TeO <sub>3</sub> )	Te metal	Te oxide (TeO <sub>4</sub> )	Te oxide (TeO <sub>3</sub> )	Te metal
H50	577.34	576.13	573.01	8.35	57.97	33.68
H70	577.33	575.82	572.83	7.02	59.69	33.29
H90	577.26	575.45	572.41	4.96	64.45	30.59
H100	577.04	575.18	571.63	4.36	69.97	25.67

Fig. 10 shows the deconvoluted high-resolution XPS spectra of Er 4p<sub>3/2</sub>. The peak which had higher BE corresponded to the Er trivalent ions (Er<sup>3+</sup>) while the peak that associated with Er metal was situated at lower BE energy. The presence of the Er<sup>3+</sup> ions were believed to promote the formation of Er-O bonds in the EDTS glass network. Like Te, the Er metal particle also consists of several Er atoms and is situated in the glass matrix at concentrations and sizes below the XRD detection limit. Fig. 10 and Table 6 indicated that the proportion of Er metal was much higher compared to the number of Er<sup>3+</sup> ions and its concentration seemed to increase with decreasing background gas pressure as more Er metal was detected in the EDTS. This is directly proportional to the overall Erbium atomic concentration reported in Table 2. Results in Table 2 clearly proves that at higher Er atomic concentration higher proportion of them nucleates and form Er nanoparticles and at lower concentrations (H100) almost 70% are present as Er<sup>3+</sup> ions. However, the variation BE for Er<sup>3+</sup> ions and Er- nanoparticles is insignificant as concentration of erbium is very low in the EDTS comparing to other components. Following the pervious argument regarding the dependence of nanoparticle size on BE, it can be concluded that there is no significant shift in the particle for Er in the studied samples. This result is significant as the presence large concentrations of Er in nanoparticle form will be detrimental for any waveguide amplifier or laser fabricated using EDTS.

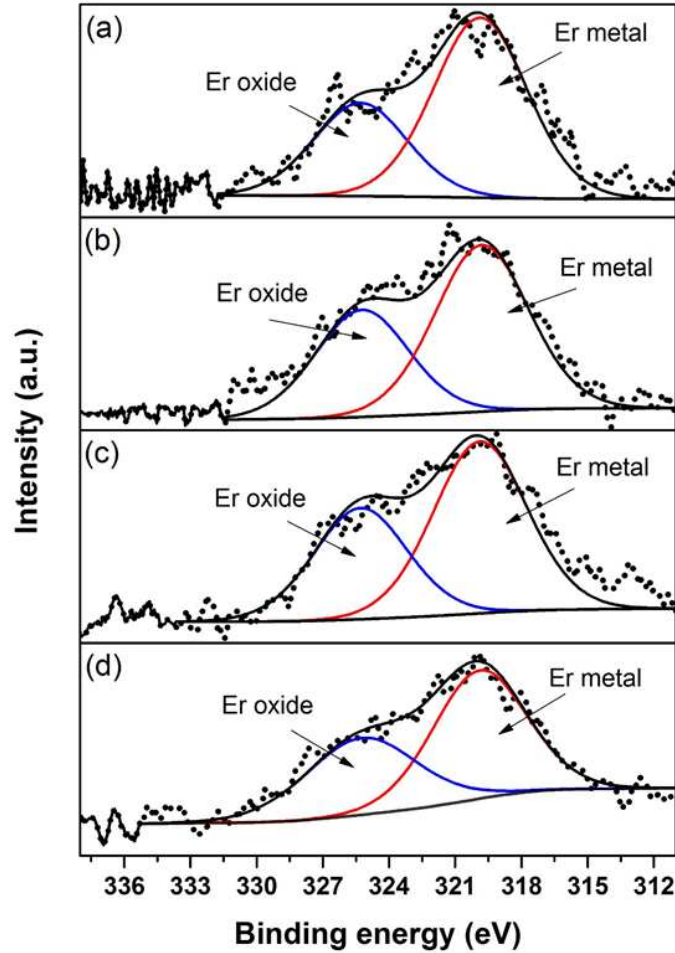


Fig. 10: Er  $4p_{3/2}$  core level spectra with peak fitting for samples prepared with oxygen gas pressure of (a) 50 mTorr (H50) (b) 70 mTorr (H70) (c) 90 mTorr (H90) (d) 100 mTorr (H100).

Table 6: Peak parameter (peak position (eV) and area percentage (%)) derived from fitting Er  $4p_{3/2}$ .

Sample	Peak position (eV)		Area (%)	
	Er oxide	Er metal	Er oxide	Er metal
H50	325.26	319.89	34.09	65.91
H70	325.29	319.88	36.02	63.98
H90	325.29	319.85	39.69	60.31
H100	325.30	319.81	41.37	58.63

Subsequently, depth profiling was done to investigate the trend of semi-quantification values as a function of etching time or EDTS depth. Fig. 11 shows the depth profile for sample H70. It was found that concentration of all the elements, except Er, which was below the detection limit, was almost consistent and this clearly showed that the distribution of elements for O, Te, Zn, Na, and Si was uniform in EDTS. Fig. 11 also shows that all elements from the tellurite

target glass mixed well with the silica. Since as the EDTS layer was too thick and the etch rate was low, the etching process did not reach the interface between EDTS and silica. Nevertheless, the depth profiling done was only survey scan at every 30 s, thus the element Er failed to be obtained.

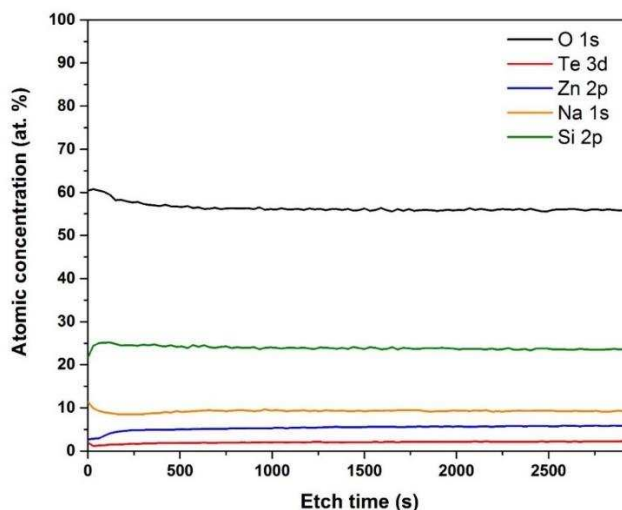


Fig. 11: XPS depth profile for sample H70. The in-depth distributions of silicon, oxygen, tellurium, zinc, and sodium are reported.

#### 4.0 Conclusion

In summary, we have studied the impact of the oxygen gas pressure towards the physical, optical, structural and chemical properties of our EDTS layers. Each parameter changes significantly altered the properties of EDTS leading to the conclusion that the background gas pressure is an important process parameter in the ULPD process for this family of glasses. Samples that were prepared using a higher background oxygen gas pressure exhibit thinner EDTS layers with lower refractive indices. Additionally, using lower  $O_2$  gas pressures increased the concentration of Te, Na, Zn and Er in the EDTS layers due to fewer collisions during the ablation and time of flight. We conclude that the oxygen pressure is an indispensable factor for the constituents of the target material to mix with silica. Furthermore, the lack of oxygen in the underlying silicon substrate caused the Te to accumulate in interphase between EDTS and silicon. Peak-fitting XPS of Te  $3d_{5/2}$  and Er  $4p_{3/2}$  revealed the presence of Te and Er metals in EDTS and, it is suggested that they are situated in interstitial sites and their size is less than 5 nm. XPS depth profiling confirms that the EDTS fabricated

using ULPD consists of a homogeneous mixture of elements from the target material and silica from the substrate.

## Acknowledgement

Authors would like to acknowledge the funding from the Engineering and Physical Sciences Research Council (EPSRC) (EP/M015165/1).

## References

- [1] Lancry M, Régnier E, Poumellec B 2012 Fictive temperature in silica-based glasses and its application to optical fiber manufacturing *Prog. Mater. Sci.* **57** 63–94.
- [2] Fanderlik I 1991 *Silica Glass and Its Application* (Prague, Elsevier).
- [3] Berwal N, Kundu R S, Nanda K, Punia R and Kishore N 2015 Physical, structural and optical characterizations of borate modified bismuth–silicate–tellurite glasses *J. Mol. Struct.* **1097** 37–44.
- [4] Righini G C et al 2009 Er<sup>3+</sup>-doped silica-hafnia films for optical waveguides and spherical resonators *J. Non. Cryst. Solids.* **355** 1853–1860.
- [5] Tosello C et al 2001 Erbium-activated silica-titania planar waveguides on silica-on-silicon substrates prepared by rf sputtering *J. Non. Cryst. Solids.* **284** 230–236.
- [6] Bouajaj A, Gonçalves R R and Ferrari M 2014 Sol-Gel-Derived Erbium-Activated Silica-Titania and Silica-Hafnia Planar Waveguides for 1.5 μm Application in C Band of Telecommunication *Spectrosc. Lett.* **47** 381–386.
- [7] Auzel F and Goldner P 2001 Towards rare-earth clustering control in doped glasses, *Opt. Mater.* **16** 93–103.
- [8] Kamil, S A, Chandrappan J, Murray M, Steenson P, Krauss T F and Jose G 2016 Ultrafast laser plasma doping of Er<sup>3+</sup> ions in silica-on-silicon for optical waveguiding applications, *Opt. Lett.* **41** (2016) 4684–4687.
- [9] Chandrappan J, Murray M, Kakkar T, Petrik P, Agocs E, Zolnai Z, Steenson D P, Jha A and Jose G 2015 Target dependent femtosecond laser plasma implantation dynamics in enabling silica for high density erbium doping *Sci. Rep.* **5** 14037.
- [10] Kashchieva E and Dimitriev Y 1995 Some peculiarities of the phase separation in the TeO<sub>2</sub>-B<sub>2</sub>O<sub>3</sub>-SiO<sub>2</sub> system *J. Mater. Sci. Lett.* **14** 732–735.
- [11] Rodrigues A C M, Keding R and Russel C 2000 Mixed former effect between TeO<sub>2</sub> and SiO<sub>2</sub> in the Li<sub>2</sub>O TeO<sub>2</sub> SiO<sub>2</sub> system *J. Non. Cryst. Solids.* **273** 53–58.
- [12] Cho D H, Choi Y G and Kim K H 2001 Improvement of <sup>4</sup>I<sub>11/2</sub> → <sup>4</sup>I<sub>13/2</sub> transition rate and thermal stabilities in Er<sup>3+</sup>-doped TeO<sub>2</sub>-B<sub>2</sub>O<sub>3</sub> (GeO<sub>2</sub>)-ZnO-K<sub>2</sub>O glasses, *ETRI J.* **23** 151–157.
- [13] Zayas M E, Espinoza-Beltran F J, Romero M and Rincon J M 1998 Preparation and characterization of new glasses from the TeO<sub>2</sub>-CdO-Al<sub>2</sub>O<sub>3</sub>-SiO<sub>2</sub> system, *J. Mater. Sci. Lett.* **17** 1099–1102.
- [14] Geohagan D B 1994 Diagnostics and characteristics of laser-produced plasmas in *Pulsed Laser Deposition of Thin Films* ed D.B. Chrisey et al (New York: John Wiley & Sons) p 115.
- [15] Kumar R, Kumar G and Umar A 2014 Pulse laser deposited nanostructured ZnO thin films: a review *J. Nanosci. Nanotechnol.* **14** 1911–1930.
- [16] Tian P, Cheng J and Zhang G 2011 X-ray photoelectron spectroscopy of Sm<sup>3+</sup>-doped CaO–MgO–Al<sub>2</sub>O<sub>3</sub>–SiO<sub>2</sub> glasses and glass ceramics, *Appl. Surf. Sci.* **257** 4896–4900.
- [17] Mekki A 2005 X-ray photoelectron spectroscopy of CeO<sub>2</sub>-Na<sub>2</sub>O-SiO<sub>2</sub> glasses *J. Electron Spectros. Relat. Phenomena.* **142** 75–81.
- [18] Wang P W and Zhang L 1996 Structural role of lead in lead silicate glasses derived

- from XPS spectra *J. Non. Cryst. Solids*. **194** 129–134.
- [19] Yamane M and Asahara Y 2004 *Glasses for Photonics* (Cambridge: Cambridge University Press).
- [20] Heese R, Chasse T and Szargan R 1999 Peak shape analysis of core level photoelectron spectra using UNIFIT for WINDOWS *Fresenius J Anal Chem* **365** 48-54.
- [21] Sharma A, Jain H and Miller A C 2001 Surface modification of a silicate glass during XPS experiments *Surf. Interface Anal.* **31** 369–374.
- [22] Serra J and Gonz P 2003 FTIR and XPS studies of bioactive silica based glasses *J. Non. Cryst. Solids*. **332** 20–27.
- [23] Eason R 2007 *Pulsed Laser Deposition of Thin Films: Applications-Led Growth of Functional Materials* (New Jersey: John Wiley & Sons).
- [24] Ryu Y R, Zhu S, Budai J D, Chandrasekhar H R, Miceli P F and White H W 2000 Optical and structural properties of ZnO films deposited on GaAs by pulsed laser deposition *J. Appl. Phys.* **88** 201–204.
- [25] Okoshi M, Kumagai H and Toyoda K 1997 Pulsed laser deposition of carbon nitride thin films in nitrogen gas ambient *J. Mater. Res.* **12** 3376–3379.
- [26] Gottmann J, Klotzbücher T and Kreutz E W 1998 Pulsed laser deposition of ceramic thin films using different laser sources *Surf. Coatings Technol.* **100–101** 411–414.
- [27] Pillonnet A, Garapon C, Champeaux C, Bovier C, Brenier R, Jaffrezic H and Mugnier J 1999 Influence of oxygen pressure on structural and optical properties of Al<sub>2</sub>O<sub>3</sub> optical waveguides prepared by pulsed laser deposition *Appl. Phys. A Mater. Sci. Process.* **69** S735–S738.
- [28] Suárez-García A, Gonzalo J and Afonso C N 2003 Low-loss Al<sub>2</sub>O<sub>3</sub> waveguides produced by pulsed laser deposition at room temperature, *Appl. Phys. A Mater. Sci. Process.* **77** 779–783.
- [29] Himpfel F J and McFeely F R, Taleb-Ibrahimi A, Yarmoff, J A, and Hollinger G 1988 Microscopic structure of the SiO<sub>2</sub>/Si interface, *Phys. Rev. B.* **38** 6084–6096.
- [30] Banaszak Holl M M and McFeely F R 1993 Si/SiO<sub>2</sub> interface: New structures and well-defined model systems, *Phys. Rev. Lett.* **71** (1993) 2441–2444.
- [31] Kovačević G and Pivac B 2014 Structure, defects, and strain in silicon-silicon oxide interfaces *J. Appl. Phys.* **115** 043531.
- [32] Wei Z, Wu S Y and Chen, X 2013 Effects of substrate temperature and ambient oxygen pressure on growth of Ba(Fe<sub>1/2</sub>Nb<sub>1/2</sub>)O<sub>3</sub> thin films by pulsed laser deposition, *Chin. Sci. Bull.* **58** 3398-3402.
- [33] Nesbitt H W, Bancroft G M, Henderson G S, Ho R, Dalby K N, Huang Y and Yan Z 2011 Bridging, non-bridging and free (O<sup>2-</sup>) oxygen in Na<sub>2</sub>O-SiO<sub>2</sub> glasses: An X-ray photoelectron spectroscopic (XPS) and nuclear magnetic resonance (NMR) study, *J. Non. Cryst. Solids*. **357** 70–180.
- [34] Mekki A, Holland D, McConville C F and Salim M 1996 An XPS study of iron sodium silicate glass surfaces *J. Non. Cryst. Solids*. **208** 267–276.
- [35] Veal B W, Lam D J and Paulikas A P 1982 XPS study of CaO in sodium silicate glass, *J. Non. Cryst. Solids*. **49** 309–320.
- [36] Edge L F, Schlom D G, Stemmer S, Lucovsky G and Luning J 2006 Detection of nanocrystallinity by X-ray absorption spectroscopy in thin film transition metal/rare-earth atom, elemental and complex oxides *Radiat. Phys. Chem.* **75** 1608–1612.
- [37] Wojcieszak R, Genet M J, Eloy P, Ruiz P and Gaigneaux E M Determination of the size of supported Pd nanoparticles by X-ray photoelectron spectroscopy. Comparison with X-ray diffraction, transmission electron microscopy, and H<sub>2</sub> chemisorption methods, *J. Phys. Chem. C.* **114** 16677–16684.
- [38] Mann T, Mathieson R, Murray M, Richards B and Jose G 2018 Femtosecond laser ablation properties of Er<sup>3+</sup> ion doped zinc-sodium tellurite glass *J. Appl. Phys.* **124** 044903.
- [39] Bukhtiyarov V I, Prosvirin I P, Kvon R I, Goncharova S N and Bal'zhinimaev B S 1997 XPS study of the size effect in ethene epoxidation on supported silver catalysts, *J. Chem. Soc. Faraday Trans.* **93** 2323–2329.

- [40] Lykhach Y et al 2016 Counting electrons on supported nanoparticles, *Nat. Mater.* **15** 284–289.
- [41] Andrade A B, Ferreira N S and Valerio M E G 2017 Particle size effects on structural and optical properties of BaF<sub>2</sub> nanoparticles *RSC Adv.* **7** 26839–26848.
- [42] Park R L 1985 Core-level spectroscopies *in Solid State Physics: Surfaces* ed R.L. Park et al (London: Academic Press) p 187.
- [43] Gantefor G 2003 Photoelectron spectroscopy *in Quantum phenomena in clusters and nanostructures* ed Khanna S N et al (Berlin: Springer) p 29-54.
- [44] Sebilliau D 2006 X-ray and electron spectroscopies: an introduction *in Magnetism: a synchrotron radiation approach* ed Beaurepaire et al (Berlin: Springer) p 15-58.
- [45] Bennett A M A, Douglas T, Unruh K M, Shah S I and Theopold K H 1994 Synthesis of III-V semiconductor particles from organometallic precursors *in Nanophase Materials: Synthesis-Properties-Applications* ed Hadjipanayis G C et al (Dordrecht: Springer) p 29-36.
- [46] Pal A, Saini P and Sapra S 2015 Conjugated-polymer/quantum-confined nanomaterials-based hybrids for optoelectronics applications *in Fundamentals of conjugated polymer blends, copolymers and composites: synthesis, properties and applications* ed Saini P (New Jersey: John Wiley & Sons) p 163-228.
- [47] Ponc V and Bond G C 1995 *Catalysis by metals and alloys* (Amsterdam: Elsevier).